Climatological Characteristics of Raindrop Size Distributions in Busan, Korea

Sung-Ho SUH[1]

Cheol-Hwan YOU[2*]

Email: youch@pknu.ac.kr

Dong-In LEE[1,2]

Institutional addresses:

[1] Department of Environmental Atmospheric Sciences, Pukyong National University, Daeyeon campus 45, Yongso-ro, Namgu, Busan 608-737 Republic of Korea

[2]Atmospheric Environmental Research Institute, Daeyeon campus 45, Yongso-ro, Namgu, Busan 608-737 Republic of Korea

* Corresponding author

Abstract

Raindrop size distribution (DSD) characteristics within the complex area of Busan, Korea (35.12°N, 129.10°E) were studied using a Precipitation Occurrence Sensor System (POSS) disdrometer over a four-year period from February 24th 2001 to December 24th 2004. Also, to find the dominant characteristics of polarized radar parameters which is differential radar reflectivity (Z_{dr}), specific differential phase (K_{dp}) and specific attenuation (A_h), T-matrix scattering simulation was applied in present study. To analyze the climatological DSD characteristics in more detail, the entire period of recorded rainfall was divided into 10 categories not only covering different temporal and spatial scales, but also different rainfall types. When only convective rainfall was considered, mean values of mass weighted mean diameter (D_m) and normalized number concentration (N_w) values for all these categories converged around a maritime cluster, except for rainfall associated with Typhoons. The convective rainfall of a Typhoon showed much smaller D_m and larger N_w compared with the other rainfall categories.

In terms of diurnal DSD variability, we analyzed maritime (continental) precipitation during the daytime (DT) (nighttime, NT), which likely results from sea (land) wind identified through wind direction analysis. These features also appeared in the seasonal diurnal distribution. The DT and NT Probability Density Function (PDF) during the Summer was similar to the PDF of the entire study period. However, the DT and NT PDF during the Winter season displayed an inverse distribution due to seasonal differences in wind direction.

Keyword: DSD, POSS disdrometer, Climatological characteristics, Land and sea wind.

1. Introduction

Raindrop Size Distribution (DSD) is controlled by the microphysical processes of rainfall and therefore it plays an important role in development of the Quantitative Precipitation Estimation (QPE) algorithms based on forward scattering simulations of radar measurements (Seliga and Bringi, 1976). DSD data accurately reflects local rainfall characteristics within an observation area (You et al., 2014). Many DSD models have been developed to characterize spatial-temporal differences in DSDs under various atmospheric conditions (Ulbrich, 1983). Marshall and Palmer (1948) developed an exponential DSD model using DSD data collected by a filter paper technique ($N(D) = 8 \times 10^3 \exp(-410R^{-0.21}D)$ in $m^{-3}mm^{-1}$, D in mm and R in mm h^{-1}). In subsequent studies, a lognormal distribution was assumed to overcome the problem of exponential DSD mismatching with real data (Mueller, 1966; Levin, 1971; Markowitz, 1976; Feingold and Levin, 1986).

To further investigate natural DSD variations, Ulbrich (1983) developed a gamma DSD that permitted changing the dimension of the intercept parameter (N_0 in $m^{-3}\ mm^{-1-\mu}$) with $N(D) = N_0 D^{\mu} \exp(-\Lambda D)$. In addition, to enable the quantitative analysis of different rainfall events, the development of a normalized gamma DSD model that accounted for the independent distribution of DSD from the disdrometer channel interval enabled a better representation of the actual DSD (Willis, 1984; Dou et al., 1999; Testud et al., 2001).

DSDs depend on the rainfall type, geographical and atmospheric conditions and observation time. Also these are closely linked to microphysical characteristics that control rainfall development mechanisms. In the case of stratiform rainfall, raindrops grow by the accretion mechanism because of the relatively long residence time in weak updraft condition, in which almost all water droplets are changed to ice particles. With time, the ice particles grow

sufficiently and fall to the ground. The raindrop size of stratiform rainfall observed at the ground level is larger than that of convective rainfall for a same rainfall intensity due to the resistance of the ice particles to break-up mechanisms. In contrast to stratiform rainfall, convective rainfall raindrops grow by the collision-coalescence mechanism associated with relatively strong vertical wind speeds and short residence time in the cloud. Fully-grown raindrops of maritime precipitation are smaller in diameter than those in stratiform rainfall due to the break-up mechanism in case of same rainfall rate (Mapes and Houze Jr, 1993; Tokay and Short, 1996). Convective rainfall can be classified into two types based on the origin and direction of movement. Rainfall systems occurring over ocean and land are referred to as maritime and continental rainfall, respectively (Göke et al., 2007). Continental rainfall is related to a cold-rain mechanism whereby raindrops grow in the form of ice particles. In contrast, maritime rainfall is related to a warm-rain mechanism whereby raindrops grow by the collision-coalescence mechanism. Therefore, the mass-weighted drop diameter (D_m) of continental rainfall observed on the ground is larger than that of maritime rainfall, and a smaller normalized intercept parameter (N_w) is observed in continental rainfall (Bringi et al., 2003).

Specific heat is a major climatological feature that creates differences between DSDs in maritime and continental regions. These two regions have different thermal capacities and thus different temperature variations are occurred with time. The surface temperature of the ocean changes slowly because of the higher thermal capacity compared with land. While the continental regions which have comparatively lower thermal capacity show greater diurnal temperature variability. Sea winds generally are occurred in from afternoon to early evening when the temperature gradient between the sea and land becomes negative, which is opposite gradient in the daytime (DT). In coastal regions, the land and sea wind effect causes a pronounced difference between the DT and nighttime (NT) DSD characteristics. Also, when

89 mountains are located near the coast, the difference is intensified by the effect of mountain and
90 valley winds (Qian, 2008).
91 In the present study, we analyzed a four-year dataset spanning from 2001 to 2004, collected
92 from Busan, Korea (35.12°N, 129.10°E) using a Precipitation Occurrence Sensor System
93 (POSS) disdrometer, to investigate the characteristics of DSDs in Busan, Korea which consist
94 complex mid-latitude region comprising both land and ocean. To quantify the effect of land
95 and sea wind on these characteristics, we also analyzed diurnal variations in DSDs. The
96 remainder of the manuscript is organized as follows. In Section 2 we review the normalized
97 gamma model and explain the DSD quality control method and the classification of rainfall. In
98 Section 3 we report the results of DSD analysis with respect to stratiform/convective and
99 continental/maritime rainfall, and discuss diurnal variations. Finally, a summary of the results
100 and the main conclusions are presented in Section 4.

101

102 **2. Data and Methods**

103 **2.1. Normalized Gamma DSD**

104 DSDs are defined by $N(D) = N_0 \exp(-\Lambda D)$ $(m^{-3}mm^{-1})$ and are reflect the microphysical
105 characteristics of rainfall using the number concentration of raindrops ($N(D)$). Also, DSDs are
106 able to calculate the many kind of parameters which show the dominant feature of raindrops.
107 Normalization is used to define the DSD and to solve the non-independence of each DSD
108 parameter (Willis, 1984; Dou et al., 1999; Testud et al., 2001). Furthermore, a normalized
109 gamma DSD enables the quantitative comparison for rainfall cases regardless of time scale and
110 rain rate. Here, we use the DSD model designed by Testud et al. (2001):

$$N(D) = N_w f(\mu)\left(\frac{D}{D_m}\right)^{\mu} \exp\left[-(4+\mu)\frac{D}{D_m}\right]. \quad (1)$$

where D is the volume equivalent spherical raindrop diameter (mm), and $f(\mu)$ is defined using the DSD model shape parameter (μ) and gamma function (Γ) as follows:

$$f(\mu) = \frac{6}{4^4}\frac{(\mu+4)^{4+\mu}}{\Gamma(4+\mu)}. \quad (2)$$

From the value of $N(D)$, the median volume diameter (D_0 in mm) can be obtained as follows:

$$\int_0^{D_0} D^3 N(D) dD = \frac{1}{2}\int_0^{D_{max}} D^3 N(D) dD. \quad (3)$$

Mass-weighted mean diameter (D_m in mm) is calculated as the ratio of the fourth to the third moment of the DSD:

$$D_m = \frac{\int_0^{D_{max}} D^4 N(D) dD}{\int_0^{D_{max}} D^3 N(D) dD}. \quad (4)$$

The normalized intercept parameter (N_w in $m^{-3}mm^{-1}$) is calculated as follows:

$$N_w = \frac{4^4}{\pi \rho_w}\left(\frac{LWC}{D_m^4}\right). \quad (5)$$

The shape of the DSD is calculated as the ratio of D_m to the standard deviation (SD) of D_m (σ_m in mm) (Ulbrich and Atlas, 1998; Bringi et al., 2003; Leinonen et al., 2012):

$$\sigma_m = \left[\frac{\int_0^{D_{max}} D^3 (D - D_m)^2 N(D) dD}{\int_0^{D_{max}} D^3 N(D) dD}\right]^{\frac{1}{2}}. \quad (6)$$

In addition, σ_m / D_m is related to μ as follows:

$$\frac{\sigma_m}{D_m} = \frac{1}{(4+\mu)^{1/2}}. \quad (7)$$

Liquid water content (LWC in g m^{-3}) can be defined from the estimated DSD:

$$LWC = \frac{\pi}{6} \rho_w \int_0^{D_{max}} D^3 N(D) dD. \quad (8)$$

where ρ_w is the water density (g m^{-3}) and it assumed as 1×10^6 g m^{-3} for a liquid. Similarly, the rainfall rate (R in mm h^{-1}) can be defined as follows:

$$R = \frac{3.6}{10^3}\frac{\pi}{6}\int_0^{D_{max}} v(D)D^3N(D)dD. \quad (9)$$

where the value of factor 3.6×10^3 is the unit conversion which converts the mass flux unit (mg m^{-2} s^{-1}) to the common unit (mm h^{-1}) for the convenience. v(D) (m s^{-1}) is the terminal velocity for each raindrop size. The relationship between v(D) and D (mm) is given by Atlas et al. (1973) who developed an empirical formula based on the data reported by Gunn and Kinzer (1949):

$$v(D) = 9.65 - 10.3\exp[-0.6D]. \quad (10)$$

2.2 Quality Control of POSS Data

POSS is used to measure the number of raindrops within the diameter range of 0.34-5.34 mm, using bistatic, continuous wave X-band Doppler radar (10.525 GHz) across 34 channels (Fig. 1; Sheppard and Joe, 2008). To estimate DSDs, Doppler power density spectrum is calculated as follows;

$$S(f) = \int_{D_{min}}^{D_{max}} N(D_m)V(D_m, \rho, h, w)\bar{S}(f, D_m, \rho, h, w)dD_m. \quad (11)$$

Where $S(f)$ means Doppler spectrum power density, $V(D_m, \rho, h, w)\bar{S}(f, D_m, \rho, h, w)$ means weighting function of $S(f)$, $\bar{S}$ is the mean of $S(f)$, ρ is density of precipitation distribution, h is the shape of precipitation distribution, $w\,(m\,s^{-1})$ is wind speed and $V(x)$ is sample volume and the symbol 'x' means arbitrary parameters which affect the sampling volume. The Doppler power density spectrum has a resolution of 16Hz and terminal velocity (v_t) has a resolution of 0.24 $m\,s^{-1}$. Transmitter and receiver skewed about 20° toward each other, and cross point of signal is located over 34 cm from transmitter-receiver. Transmitter-receiver toward upper side detects $N(D)$ in $V(x)$ (Sheppard, 1990). Also, Sheppard (1990) and Sheppard and Joe (1994) noted some shortcomings as the overestimation of small drops at horizontal wind larger than 6 $m\,s^{-1}$. However, in present study, the quality control of POSS for wind effect was not considered because it lies beyond this work. Detailed specifications and measurement ranges and raindrop sizes for each observation channel of the POSS disdrometer are summarized in Table 1.

A POSS disdrometer have been operating in Busan, Korea (35.12°N, 129.10°E), along with other atmospheric instruments, the locations of which are shown in Fig. 2. Estimating raindrop diameter correctly is challenging and care should be taken to ensure reliable data are collected. We performed the following quality controls to optimize the accuracy of the disdrometer estimates. i) Non-liquid type event data (e.g., snow, hail etc.) detected by POSS were excluded by routine observation and surface weather chart provided by Korea Meteorological Administration (KMA). ii) DSD spectra in which drops were not found in at least five

consecutive channels were removed as non-atmospheric. iii) Only data recorded in more than 10 complete channels were considered. iv) To compensate for the reduced capability to detect raindrops smaller than 1 mm when R > 200 mm h^{-1} (as recorded by the disdrometer), data for R>200 mm h^{-1} were not included in the analyses, even though the number of samples was only 64 for the entire period. v) To eliminate wind and acoustic noise, data collected when R < 0.1 mm h^{-1} are removed (Tokay and Short, 1996).

After performing all quality control procedures, 99,388 spectra were left from original data (166,682) for 1-min temporal resolution. Accumulated rainfall amount from POSS during the entire period was 4261.49 mm. To verify the reliability of the POSS data, they were compared with data collected by a 0.5 mm tipping bucket rain gaugeat an automatic weather system (AWS) located ~368 m from the POSS (Fig. 3).

2.3 Radar Parameters

First, the radar reflectivity factor (z in mm^6m^{-3}) and non-polarized radar reflectivity (Z in dBZ) were computed using the DSD data collected by POSS, as follows:

$$z = \int_0^{D_{max}} D^6 N(D) dD. \quad (12)$$

$$Z = 10\log_{10}(z). \quad (13)$$

The T-matrix method used in this study is initially proposed by Waterman (1965, 1971) to

calculate electromagnetic scattering by single non-spherical raindrops. The adaptable parameters for this calculation are frequency, temperature, hydrometeor types, raindrop's canting angle and axis ratio (γ) and explained the following sentences. Axis ratios of raindrops differ with atmospheric conditions and rainfall type. To derive the drop shape relation from the drop diameter, we applied the results of numerical simulations and wind tunnel tests employing a forth-polynomial equation, as in many previous studies (Beard and Chuang, 1987; Pruppacher and Beard, 1970; Andsager et al., 1999; Brandes et al., 2002). The axis ratio relation used in the present study is a combination of those from Andsager et al. (1999) and Beard and Chuang (1987) for three raindrop size ranges (Bringi et al., 2003).

The raindrop axis ratio relation of Andsager et al. (1999) is applied in the range of $1 < D\,(\mathrm{mm}) < 4$, as follows:

$$r = 1.0048 + 0.0057D - 2.628D^2 + 3.682D^3 - 1.677D^4. \quad (14)$$

The drop-shape relation of Beard and Chuang (1987) is applied in the range of $D < 1$ mm and $D > 4$ mm, as follows:

$$r = 1.012 + 0.01445D - 0.01028D^2. \quad (15)$$

We assumed SD and the mean canting angle of raindrops as 7° and 0°, respectively. The refractive indices of liquid water at 20 ℃ were used (Ray, 1972). Also, the condition of

frequency for electromagnetic wave of radar is 2.85 GHz (S-band). We calculated dual polarized radar parameters based on these conditions. The parameters of differential reflectivity (Z_{dr} in dB), specific differential phase (K_{dp} in $\deg km^{-1}$), and attenuation (A_h in $dB\ km^{-1}$), using DSD data were calculated and analyzed.

2.4. Classification of Rainfall Types and Rainfall Events

Rainfall systems can be classified as stratiform or convective in nature, via analysis of the following microphysical characteristics: i) DSD, using relationships between N_0 and R ($N_0 > 4 \times 10^9 R^{-4.3}$ in $m^{-3}mm^{-1}$ is considered as convective rainfall, Tokay and Short, 1996; Testud et al., 2001); ii) Z, where, according to Gamache and Houze (1982), a rainfall system that displays radar reflectivity larger than 38 dBZ is considered to be convective; and iii) R, where average value larger than 0.5 mm per 5 min is considered as convective rainfall (Johnson and Hamilton, 1988). Alternatively, rainfall that has 1-min $R > 5\ (0.5)\ mm\ h^{-1}$ and a SD of $R > (<)\ 1.5\ mm\ h^{-1}$ is considered as convective (stratiform) type (Bringi et al., 2003). The rainfall classification method proposed by Bringi et al. (2003) is applied in the present study.

It is necessary to categorize different rainfall systems because their microphysical characteristics show great variation depending on the type of rainfall, as well as the type of rainfall event; e.g., Typhoon, Changma, heavy rainfall and seasonally discrete rainfall. To investigate the temporal variation in DSDs, we analyzed daily and seasonal DSDs. Likewise, to investigate diurnal variability in DSD, DT and NT data were considered by using the sunrise and sunset time in Busan (provided by the Korea Astronomy and Space Science Institute [KASI]). In the middle latitudes, and including Busan, the timings of sunrise and sunset vary due to solar culminating height. The earliest and latest sunrise (sunset) time of the entire period

252 is 0509 KST (1712 KST) and 0733 KST (1942 KST), respectively. DT (NT) is defined as the
253 period from the latest sunrise (sunset) time to the earliest sunset (sunrise) time for the unity of
254 classification of each time group (Table 2).
255 To analyze the predominant characteristics of DSDs for Typhoon rainfall, nine Typhoon events
256 were selected from throughout the entire study period which is summarized in Table 2.
257 This study utilizes KMA rainfall warning regulations to identify heavy rainfall events. The
258 KMA issues a warning if the accumulated rain amount is expected to be >70 mm within a 6-
259 hour period, or >110 mm within a 12-hour period. Rainfall events classified as Changma and
260 Typhoon were not included in the classification 'heavy rainfall'.
261 Changma is the localized rainfall system or rainy season that is usually present over the Korean
262 Peninsula between mid-June and mid-July which is similar to the Meiyu (China) or Baiu
263 (Japan). The selected dates and periods of each rainfall category are summarized in Table 2.

264

265 **3. Results**

266 **3.1. DSD and Radar Parameters**

267 Figure 4 shows the Probability Density Function (PDF) and Cumulative Distribution Function
268 (CDF) of DSDs and radar parameters with respect to the entire, stratiform and convective
269 rainfall. The PDFs of DSD and radar parameters were calculated using the non-
270 parameterization kernel estimation to identify the dominant distribution of each parameter
271 recorded in Busan. Non-parameterization kernel estimation was also used to identify
272 continuous distributions of DSDs. The PDF of stratiform rainfall is more similar to that of the
273 dataset for the entire analysis period due to the dominant contribution of stratiform rainfall

(about 62.93%) to the overall rainfall than that of convective rainfall. However, the PDF for convective rainfall is significantly different from that of the entire analysis period, and as the convective rainfall contributes only 6.11% of the overall rainfall (Table 3). When $\mu < 0$ the distribution of μ for convective rain has more value of PDF than that for stratiform rain (Fig. 4a). Alternatively, the frequency of μ for stratiform rainfall is higher than that of convective rainfall when $0 < \mu < 5$. The value of μ for convective rainfall is higher than that for stratiform rainfall because the break-up mechanism would be increase the number concentration of small raindrops. The number concentrations of mid-size raindrops increased due to the decrease in the number concentration of relatively large raindrops (Hu and Srivastava, 1995; Sauvageot and Lacaux, 1995). However, we observed a higher frequency of convective rainfall than stratiform rainfall in the negative μ range.

The PDF of D_m displays peak around 1.2 and 1.4 mm for stratiform rainfall and the entire rainfall dataset, respectively. We note that a gentle peak exists around 0.7 mm for both stratiform and convective rainfall datasets (Fig. 4b). These features are similar to the distribution of D_m observed in a high-latitude region at Järvenpää, Finland (Fig. 4 of Leinonen et al., 2012). For D_m values > 1.7 mm, the PDF for convective rainfall is higher than stratiform rainfall. Accordingly, the value of DSD for stratiform rainfall is higher than that of convective rainfall when $D_m < 1.7$ mm. Generally, stratiform rainfall that develops by the cold rain process displays weaker upward winds and less efficient break-up of raindrops. Therefore, in the same rainfall rate, stratiform rainfall tends to produce larger raindrops than convective rainfall that develops by the warm rain process. However, the average D_m values for convective and stratiform rain for the entire period are approximately 1.45 and 1.7 mm,

296 respectively. In short, D_m is proportional to R regardless of rainfall type. This finding is
297 consistent with the results of Atlas et al. (1999) who found that the D_m of convective rainfall
298 is larger than that of stratiform rainfall on Kapingamarangi Island, Micronesia.
299 The PDF of $\log_{10}(N_w)$ for the entire rainfall dataset was evenly distributed between 1.5 and
300 5.5, with a peak at N_w = 3.3 (Fig. 4c). The PDF of $\log_{10}(N_w)$ for stratiform rainfall is rarely
301 > 5.5, while for convective rainfall it is higher at > 5.5 than that of stratiform. There is a similar
302 frequency in the stratiform and convective rainfall at 4.4.
303 The PDF distributions for $\log_{10}(R)$ and $\log_{10}(LWC)$ are similar each other (Fig. 4d and e).
304 It is inferred that the similar results come from the using of alike moment of DSD as 3.67 and
305 3 for R and LWC, respectively. The PDF of $\log_{10}(R)$ for the entire rainfall dataset ranged
306 between -0.5 and 2. A peak exists at 0.3 and the PDF rapidly decreases from the peak value as
307 R increases. The PDF for stratiform rainfall has a higher frequency than that of the entire
308 rainfall when $-0.3 < \log_{10}(R) < 0.7$, while the PDF for convective rainfall is denser between
309 0.4 and 2. Furthermore, the frequency of the PDF for convective rainfall was higher than that
310 of stratiform rainfall in case of $\log_{10}(R) > 0.65$ and the peak value shown as 0.9.
311 The PDF and CDF for Z, Z_{dr}, K_{dp} and A_h are shown in Fig. 4f-i. The PDF of Z for
312 stratiform rainfall (Fig. 4f) is widely distributed between 10 and 50 dBZ with the peak at
313 approximately 27 dBZ. Conversely, for convective rainfall, the value of PDF lie between 27
314 and 55 dBZ and the peak frequency value at approximately 41 dBZ. The frequency value of
315 reflectivity is higher for convective rainfall than for stratiform rainfall in the range of ~ >35
316 dBZ. Furthermore, the shape of the PDF for convective rainfall is similar to that reported for
317 Darwin, Australia (Steiner et al., 1995); however, for stratiform rainfall there are significant
318 differences between Busan and Darwin in terms of the shape of the frequency distribution. The

PDF of Z_{dr} for the entire rainfall primarily exists between 0 and 2.5 dB, and the peaks are at 0.3 and 1.8 dB (Fig. 4g). The distribution of Z_{dr} for convective and stratiform rainfall is concentrated between 0.6 and 1.6 dB, and between 0.3 and 2 dB, respectively. The frequency of Z_{dr} for convective (stratiform) rainfall exists in ranges higher (lower) than stratiform (convective) at 0.9 dB.

The dominant distribution of K_{dp} for the entire dataset and for stratiform rainfall lies between 0 and 0.14 deg km^{-1}, with a peak value of 0.03 deg km^{-1} and 0.08 deg km^{-1}. However, for convective rainfall the PDF of K_{dp} is evenly exist between 0.01 and 0.15 deg km^{-1}. Furthermore, when K_{dp} > 0.056 deg km^{-1}, the frequency of the PDF for convective rainfall is higher than that of stratiform rainfall (Fig. 4h).

The PDF of A_h is similar to that of K_{dp} and is exist between 0 and 0.01 dB km^{-1}. For the case of the entire rainfall dataset and for stratiform rainfall, the PDF of A_h is concentrated between 0 and 2.0×10^{-3} dB km^{-1} and that of convective rainfall is strongly concentrated between 1.0×10^{-3} and 8.0×10^{-3} dB km^{-1} (Fig. 4i). Unlike the PDF of A_h for convective rainfall, the PDF for stratiform rainfall shows a strong peak at about 7.0×10^{-4} dB km^{-1}.

3.2. Climatological Characteristics of DSD in Busan

The climatological characteristics of DSDs for 10 rainfall categories are analyzed in this study. Sample size and ratio rainfall for each category are summarized in Table 3. Figure 5a illustrates the distribution of all 1-min stratiform rainfall data, and Fig. 5b shows scatter plots of averaged D_m and $\log_{10}(N_w)$ for all 10 rainfall categories for stratiform rainfall data. Figure 5a displays a remarkable clear boundary in the bottom sector and shows that most of the data lie below the

342 reference line used by Bringi et al. (2003) to classify convective and stratiform rainfall. The
343 average value of D_m and $\log_{10}(N_w)$ for all rainfall categories, except for heavy rainfall,
344 exist between 1.4 mm and 1.6 mm and between 3.15 and 3.5, respectively (Fig. 5b). These
345 values are relatively small compared with the reference line presented by Bringi et al. (2003).
346 The distribution of 1-min convective rainfall data is displayed in Fig. 6a and the distribution of
347 average values of D_m and N_w for the 10 rainfall categories in the case of convective rainfall
348 in Fig. 6b. The blue and red plus symbols represent maritime and continental rainfall,
349 respectively, as defined by Bringi et al. (2003). The scatter plot of 1-min convective rainfall
350 data shows more in the continental cluster than the maritime cluster; however, the average
351 values for the 10 rainfall categories are all located around the maritime cluster, except for the
352 Typhoon category. By considering the entire average values including Typhoon event (Fig. 6b),
353 we can induce the simple linear equation using D_m and $\log_{10}(N_w)$ as follows:

354

355 $$\log_{10}(N_w) = -1.8D_m + 6.9. \quad (16)$$

356

357 Even the coefficients in Eq. 16 might be changed slightly with the Typhoon values, this result
358 does not represent in D_m < 1.2 mm and D_m > 1.9 mm. The D_m (N_w) value for the Typhoon
359 category was considerably smaller (larger) than that of the other categories as well as that of
360 stratiform type of Typhoon. This result does not agree with that reported by Chang et al. (2009),
361 who noted that the D_m of convective rainfall Typhoon showed a large value compared with
362 that associated with stratiform rainfall.

363

3.3 Diurnal Variation in Raindrop Size Distributions

3.3.1. Diurnal Variations in DSDs

Figure 7a shows a histogram of normalized frequency of 16 wind directions recorded by the AWS, which is the same instrument as that used to collect the data shown in Fig. 3. To establish the existence of a land and sea wind, the difference in wind direction frequencies between DT and NT were analyzed. Figure 7b shows the difference between DT and NT, difference frequency means normalized frequency of wind direction for DT subtract to that of NT for each direction, in terms of the normalized frequency of 16 wind directions. In other word, positive (negative) values indicate that the frequency of wind is more often observed during DT (NT). Also, land (sea) wind defined in present study from 225° (45°) to 45° (225°) according to the geographical condition in Busan. The predominant frequency of wind direction in the DT (NT), between 205° (22.5°) and 22.5° (205.5°), is higher than that in the NT (DT) (Fig. 7b). The observation site where the POSS was installed at western side from the closest coast line, distance is about 611 m, suggesting that the effect of the land and sea wind would have been recorded.To understand the effects of the land and sea wind on DSD characteristics, we analyzed the PDF and 2-hour averaged DSD parameters for DT and NT. Figure 8 illustrates the distributions of μ, D_m, $\log_{10}(N_w)$, $\log_{10}(LWC)$, $\log_{10}(R)$, and Z. There were large variations of μ with time. The μ values varied from 2.41 to 3.17 and the minimum and maximum μ values occurred at 0800 KST and 1200 KST, respectively (Fig. 8a). A D_m larger than 1.3 mm dominated from 0000 KST to 1200 KST, before decreasing remarkably between 1200 and 1400 KST. The minimum and maximum D_m appeared at 1400 KST and 0800 KST, respectively (Fig. 8b).

386 N_w distribution showed inversely to D_m; however, no inverse relationship was identified
387 between D_m and N_w in case of the time series (Fig. 8c). The maximum and minimum values
388 of N_w were found at 0600 KST and 2200 KST.
389 Variability through time was similar for R, LWC, and Z_h as D_m. There was an increasing
390 trend from 0000 KST to 0800 KST followed by a remarkably decreasing trend from 0800 KST
391 to 1400 KST (Figs 8d, 11e and 11f). Note that the time of the sharp decline for R between
392 1200 KST and 1400 KST is simultaneous with a D_m decrease. Larger (smaller) drops would
393 contribute to higher R in the morning (afternoon). These variations considerably matched
394 with the diurnal sea wind time series (Fig. 8g). Sea wind is the sum value of normalized wind
395 frequency between 45° and 225°. From 0200 (1400) KST to 1200 (2000) KST shows smaller
396 (larger) value of sea wind frequency which is opposite to the relatively larger (smaller) parts of
397 each parameter (D_m, R, LWC and Z_h).
398 The PDF distribution of μ between -2 and 0 is more concentrated for NT than for DT.
399 Furthermore, when μ > 0, DT and NT frequency distributions are similar (Fig. 9a). A larger
400 $N(D)$ of small or large raindrops would be expected in NT than in DT.
401 The distribution of DT D_m < 0.7 mm is wider than that of the NT. However, between 0.7
402 and 1.5 mm the frequency for NT is higher than that for DT, whereas the distribution in the
403 range D_m > 1.5 mm is similar for both DT and NT (Fig. 9b). We note that the smaller peak
404 of D_m around 0.6 mm for the entire rainfall dataset (Fig. 4b) was observed only in DT.
405 The distribution of $log_{10}(N_w)$ for DT has higher value of PDF at larger $log_{10}(N_w)$ than that
406 of NT at $log_{10}(N_w)$ > 4 (Fig. 9c).
407 Bringi et al. (2003) noted that the maritime climatology displayed larger N_w and smaller D_m
408 values than the continental climatology, based on observed DSDs in the low and middle latitude.

Also, Göke et al. (2007) emphasized that rainfall type can be defined by the origin location and movement direction. In accordance with these previous results, we consider NT rainfall in the Busan region to be more likely caused by a continental convective system.

In the present study, the shape of the PDF of LWC and R for DT and NT are similar which is the same reason with the results of Fig. 4e-f. LWC and R distributions during the DT (NT) are higher (lower) than in the NT (DT) when $log_{10}(LWC)$ and $log_{10}(R)$ are larger (smaller) than -1.2 and 0, respectively (Fig. 9d and e). Z has similar pattern with LWC and R during the DT (NT) was higher (lower) than in the NT (DT) in the range below (above) about 27 dBZ (Fig. 9f).

3.3.2. Diurnal Variations of DSDs with respect to Season

Busan experiences distinct atmospheric conditions that are caused by the different frequencies and magnitudes of land and sea winds in response to variable sunrise and sunset times. To identify seasonal variations of DSDs with respect to the effect of the land and sea wind, we analyzed the DT and NT PDF of D_m and N_w in the Summer and Winter. The start and end times of DT (NT) were sorted using the latest sunrise (sunset) and the earliest sunset (sunrise) time for each season (Table 4) which is same method that of entire period classification.

Figure 10a shows a histogram of wind directions in Summer (light grey) and Winter (dark grey). The frequencies of Summer and Winter wind directions are similar to each other. However, in Fig. 10b, the DT and NT distributions of Winter wind direction display opposing frequencies. Note that Winter season shows remarkable frequency of land (sea) wind between 0° (157.5°) and 45° (202.5°) at DT (NT) compared with results of those for Summer season. The accumulated value of normalized wind frequencies at the sea and land wind show different

feature between Summer and Winter season (Table 5).

To identify the variability of DSDs caused by the land and sea wind in Summer and Winter, a 2-hour interval time series of D_m, N_w and R was analyzed. In the Summer, the time series of D_m displays considerably large values between 0000 KST and 1200 KST, compared with the period between 1400 KST and 2200 KST (Fig. 11a). The mean value of D_m decreases dramatically between 1200 KST and 1400 KST. $log_{10}(N_w)$ has a negative relationship with D_m (Fig. 11b). However, the inverse relation between $log_{10}(N_w)$ and D_m is not remarkable. $log_{10}(R)$ tends to increase gradually from 0000 KST to 0800 KST and decrease from 0800 KST to 1400 KST, which is similar to the pattern that of entire period (Fig. 11c). Kozu et al. (2006) analyzed the diurnal variation in R at Gadanki (South India), Singapore, and Kototabang (West Sumatra) during the Summer monsoon season. All regions displayed maximum R at approximately 1600 LST, except for Gadanki. Also, Qian (2008), who analyzed the diurnal variability of wind direction and R on Java Island during the Summer season using 30 years (from 1971 to 2000) of NCEP/NCAR reanalyzed data. They found that a land wind occurred from 0100 LST to 1000 LST and a sea wind from 1300 LST to 2200 LST (Fig. 7 of Qian (2008)). Normalized wind frequency for each direction is similar pattern to the results of Qian (2008) but pattern of R is different with that of Kozu et al. (2006). The diurnal variation of rain rate in the present study from 0200 (1200) KST to 1000 (2000) KST shows relatively smaller (larger) frequencies of sea wind. It is different pattern with the result of Kozu et al. (2006). However, these patterns matched with the time series of D_m and $log_{10}(N_w)$. Larger frequency of sea wind direction shows counter-proportional (proportional) relationship to the smaller (larger) frequency of D_m ($log_{10}(N_w)$).

Variability of D_m time series for Winter is the inverse of the Summer time series (Fig. 11a).

455 The mean value of D_m steadily increases from 0000 KST to 1600 KST and then decreases
456 from 1600 KST to 2200 KST. The Winter $log_{10}(N_w)$ time series displays a clear inverse
457 pattern compared with the D_m variation with time and increases from 1600 KST to 0400 KST
458 and then steadily decreases from 0400 KST to 1600 KST (Fig. 11b). The peak of $log_{10}(N_w)$
459 occurs at 0400 KST. However, the time series of $log_{10}(R)$ for Winter season shows similar
460 pattern with that of Summer unlike to another parameters (Fig. 11c). Based on the diurnal
461 variation of R, the variations of D_m and N_w would be independent to R.
462 Alike to the D_m and $log_{10}(N_w)$, normalized wind frequency of wind direction for Winter
463 season shows inverse relationship to that of Summer season (Fig. 11d). The value of frequency
464 generally decreases (increases) from 0400 (1400) KST to 1400 (0400) KST. Also, it shows
465 symmetry pattern with that of Summer season.
466 The PDF distribution of Summer D_m displays a relatively large DT frequency compared with
467 NT when D_m < 1.65 mm, except for the range between 0.6 and 0.9 mm. However, in the
468 range of D_m > 1.65 mm, the NT PDF displays a larger frequency (Fig. 12a). The PDF of
469 $log_{10}(N_w)$ for DT (NT) has a larger frequency than the NT (DT) when $log_{10}(N_w)$ > (<) 3.3
470 but smaller frequency when $log_{10}(N_w)$ < (>) 3.3 (Fig. 12c).
471 The DT and NT PDFs of D_m and $log_{10}(N_w)$ during Winter display an inverse distribution
472 to that of Summer. For the PDF of D_m, there is a considerable frequency for NT (DT) when
473 D_m < (>) 1.6 mm (Fig. 12b). The PDF of $log_{10}(N_w)$ of Summer season for NT (DT) is
474 larger than that of the DT when $log_{10}(N_w)$ < (>) 3.5 (Fig. 12d). In the PDF analysis, relatively
475 large (small) D_m and small (large) $log_{10}(N_w)$ are displayed during the NT (DT) when a land
476 wind (sea wind) occurs.
477 Bringi et al. (2003) referred that the convective rainfall type is able to be classified as the

478 continental and maritime-like precipitation using D_m and N_w. As the previous study result, we
479 analyzed the PDF of DSDs for Summer and Winter with respect to convective rainfall type.
480 These feature would be shown more clearly in convective type. The convective rainfall type of
481 PDFs of DT and NT for Summer show similar shape of distribution to that of all rainfall type
482 (Fig. 3a). For the PDF of D_m, there is a more frequency for DT (NT) than NT (DT) when D_m
483 < (>) 2.0 mm except for between 0.7 mm and 1.2 mm (Fig. 13a). The PDF of convective
484 rainfall type's $log_{10}(N_w)$ for DT (NT) has a larger frequency than the NT (DT) when
485 $log_{10}(N_w)$ > (<) 3.4 except for between 4.3 and 5.5 (Fig. 12c). PDF distributions for Winter
486 season show more clear pattern compared with those of the entire rainfall type. The value of
487 PDF for D_m in DT (NT) have considerably larger than NT (DT) when D_m > (<) 1.9 mm,
488 especially between 2.15 mm and 2.3 mm (Fig. 13b). Also, those for $\log_{10}(N_w)$ in DT (NT)
489 show dramatic values when $\log_{10}(N_w)$ < (>) 3.6. Furthermore, PDF values significantly
490 concentrated on between 3 < $\log_{10}(N_w)$ < 3.2 (Fig. 13d). In short, considering the DSD
491 parameters with wind directions, the maritime (continental)-like precipitation would depend
492 on the sea (land) wind.

493

494 **4. Summary and Conclusion**

495 Climatological characteristics of DSDs in Busan were analyzed using the DSD data observed
496 by POSS over a four-year period from February 24th 2001 to December 24th 2004. Observed
497 DSDs were filtered to remove errors by performing several quality control measures, and an
498 AWS rain gauge installed nearby was used to verify the rainfall amount recorded by the POSS.
499 We analyzed DSD characteristics of convective and stratiform rainfall types, as defined by
500 Bringi et al. (2003). The rainfall dataset was thus divided into stratiform and convective rainfall

and their contributions to the total rainfall were 62.93% and 6.11%, respectively. Also, to find the climatological characteristics of DSD for rainfall case, the entire rainfall data was classified as 10 rainfall categories including the entire period case.

According to the study by Bringi et al. (2003), the rainfall in Busan shows maritime climatological DSD characteristics. The mean values of D_m and N_w for stratiform rainfall are relatively small compared with the average line of stratiform rainfall produced by Bringi et al. (2003), except for heavy rainfall events. In case of convective type, mean values of D_m and N_w are converged around the maritime cluster, except for the Typhoon category. The convective rainfall associated with a Typhoon has considerably smaller D_m and larger N_w values compared with the other rainfall categories. This is likely caused by increased raindrop break-up mechanism as a result of strong wind effects. Furthermore, the distributions of mean D_m and N_w values for all rainfall categories associated with convective rainfall displays a linear relationship including the Typhoon category.

The analysis of diurnal variation in DSD yielded the following results: first, the frequency of μ is higher at NT than during the DT in the negative value. The PDF of R is higher at NT than during the DT when $\log_{10}(R) > 0.6$. The value of PDF for D_m during DT is larger than NT smaller than 0.65 mm. For N_w, which tends to be inversely related to D_m, its frequency is higher at NT than DT when $\log_{10}(N_w) > 3.8$. This feature is matched with the time series of normalized frequency of sea wind which shows inverse relationship to D_m. Smaller D_m corresponds to the larger sea wind frequency. In short, maritime (continental) –like precipitation are observed in the DT (NT) more often than in the NT (DT) according to the features of wind. The above-mentioned DSD characteristics are likely due to the land and sea wind caused by differences in specific heat between the land and ocean. These features are also apparent in the seasonal diurnal distribution. The PDF of DT and NT for convective rainfall type during the Summer is

similar to the PDF of the entire period; however, those of the Winter displays the significant inverse distribution compared to the Summer because of obvious seasonal differences in wind direction.

Author contributions

Cheol-Hwan You designed the study. Sung-Ho Suh modified the original study theme and performed the study. Cheol-Hwan You and Sung-Ho Suh performed research, obtained the results and prepared the manuscript along with contributions from all of the co-authors. Dong-In Lee examined the results and checked the manuscript.

Acknowledgement

This work was funded by the Korea Meteorological Industry Promotion Agency under Grant KMIPA 2015-1050. The authors acknowledge providing, weather chart, and AWS data for this work from the Korea Meteorological Administration. The authors also acknowledge providing codes for scattering simulation from Professor V. N. Bringi at Colorado State University.

564 **References**

565 Andsager, K., Beard, K. V., and Laird, N. F.: Laboratory measurements of axis ratios for large
566 raindrops, Journal of the Atmospheric Sciences, 56, 2673-2683, 1999.
567 Atlas, D., Srivastava, R., and Sekhon, R. S.: Doppler radar characteristics of precipitation at
568 vertical incidence, Reviews of Geophysics, 11, 1-35, 1973.
569 Atlas, D., Ulbrich, C. W., Marks, F. D., Amitai, E., and Williams, C. R.: Systematic variation
570 of drop size and radar-rainfall relations, Journal of Geophysical Research: Atmospheres (1984–
571 2012), 104, 6155-6169, 1999.
572 Beard, K. V., and Chuang, C.: A new model for the equilibrium shape of raindrops, Journal of
573 the Atmospheric sciences, 44, 1509-1524, 1987.
574 Brandes, E. A., Zhang, G., and Vivekanandan, J.: Experiments in rainfall estimation with a
575 polarimetric radar in a subtropical environment, Journal of Applied Meteorology, 41, 674-685,
576 2002.
577 Bringi, V., Chandrasekar, V., Hubbert, J., Gorgucci, E., Randeu, W., and Schoenhuber, M.:
578 Raindrop size distribution in different climatic regimes from disdrometer and dual-polarized
579 radar analysis, Journal of the atmospheric sciences, 60, 354-365, 2003.
580 Chang, W.-Y., Wang, T.-C. C., and Lin, P.-L.: Characteristics of the raindrop size distribution
581 and drop shape relation in Typhoon systems in the western Pacific from the 2D video
582 disdrometer and NCU C-band polarimetric radar, Journal of Atmospheric and Oceanic
583 Technology, 26, 1973-1993, 2009.
584 Dou, X., Testud, J., Amayenc, P., and Black, R.: The parameterization of rain for a weather
585 radar, Comptes Rendus de l'Académie des Sciences-Series IIA-Earth and Planetary Science,
586 328, 577-582, 1999.

587 Feingold, G., and Levin, Z.: The lognormal fit to raindrop spectra from frontal convective
588 clouds in Israel, Journal of Climate and Applied Meteorology, 25, 1346-1363, 1986.
589 Göke, S., Ochs III, H. T., and Rauber, R. M.: Radar analysis of precipitation initiation in
590 maritime versus continental clouds near the Florida coast: Inferences concerning the role of
591 CCN and giant nuclei, Journal of the Atmospheric Sciences, 64, 3695-3707, 2007.
592 Gamache, J. F., and Houze Jr, R. A.: Mesoscale air motions associated with a tropical squall
593 line, Monthly Weather Review, 110, 118-135, 1982.
594 Gunn, R., and Kinzer, G. D.: The terminal velocity of fall for water droplets in stagnant air,
595 Journal of Meteorology, 6, 243-248, 1949.
596 Hu, Z., and Srivastava, R.: Evolution of raindrop size distribution by coalescence, breakup, and
597 evaporation: Theory and observations, Journal of the atmospheric sciences, 52, 1761-1783,
598 1995.
599 Johnson, R. H., and Hamilton, P. J.: The relationship of surface pressure features to the
600 precipitation and airflow structure of an intense midlatitude squall line, Monthly Weather
601 Review, 116, 1444-1473, 1988.
602 Kozu, T., Reddy, K. K., Mori, S., Thurai, M., Ong, J. T., Rao, D. N., and Shimomai, T.: Seasonal
603 and diurnal variations of raindrop size distribution in Asian monsoon region, JOURNAL-
604 METEOROLOGICAL SOCIETY OF JAPAN SERIES 2, 84, 195, 2006.
605 Leinonen, J., Moisseev, D., Leskinen, M., and Petersen, W. A.: A climatology of disdrometer
606 measurements of rainfall in Finland over five years with implications for global radar
607 observations, Journal of Applied Meteorology and Climatology, 51, 392-404, 2012.
608 Levin, Z.: Charge separation by splashing of naturally falling raindrops, Journal of the
609 Atmospheric Sciences, 28, 543-548, 1971.
610 Mapes, B. E., and Houze Jr, R. A.: Cloud clusters and superclusters over the oceanic warm

611 pool, Monthly Weather Review, 121, 1398-1416, 1993.
612 Markowitz, A. H.: Raindrop size distribution expressions, Journal of Applied Meteorology, 15,
613 1029-1031, 1976.
614 Marshall, J. S., and Palmer, W. M. K.: The distribution of raindrops with size, Journal of
615 meteorology, 5, 165-166, 1948.
616 Mueller, E. A.: Radar cross sections from drop size spectra, University of Illinois at Urbana-
617 Champaign, 1966.
618 Pruppacher, H., and Beard, K.: A wind tunnel investigation of the internal circulation and shape
619 of water drops falling at terminal velocity in air, Quarterly Journal of the Royal Meteorological
620 Society, 96, 247-256, 1970.
621 Qian, J.-H.: Why precipitation is mostly concentrated over islands in the Maritime Continent,
622 Journal of the Atmospheric Sciences, 65, 1428-1441, 2008.
623 Ray, P. S.: Broadband complex refractive indices of ice and water, Applied Optics, 11, 1836-
624 1844, 1972.
625 Sauvageot, H., and Lacaux, J.-P.: The shape of averaged drop size distributions, Journal of the
626 Atmospheric Sciences, 52, 1070-1083, 1995.
627 Seliga, T., and Bringi, V.: Potential use of radar differential reflectivity measurements at
628 orthogonal polarizations for measuring precipitation, Journal of Applied Meteorology, 15, 69-
629 76, 1976.
630 Sheppard, B. E.: Measurement of raindrop size distributions using a small Doppler radar. J.
631 Atmos. Oceanic Technol., 7, 255–268, 1990.
632 Sheppard, B. E. and P. I. Joe: Comparison of raindrop size distribution measurements by a
633 Joss–Waldvogel disdrometer, a PMS 2DG spectrometer and a POSS Doppler radar. J. Atmos.
634 Oceanic Technol., 11, 874–887, 1994.

635 Sheppard, B., and Joe, P.: Performance of the precipitation occurrence sensor system as a
636 precipitation gauge, Journal of atmospheric and Oceanic technology, 25, 196-212, 2008.
637 Steiner, M., Houze Jr, R. A., and Yuter, S. E.: Climatological characterization of three-
638 dimensional storm structure from operational radar and rain gauge data, Journal of Applied
639 Meteorology, 34, 1978-2007, 1995.
640 Testud, J., Oury, S., Black, R. A., Amayenc, P., and Dou, X.: The concept of "normalized"
641 distribution to describe raindrop spectra: A tool for cloud physics and cloud remote sensing,
642 Journal of Applied Meteorology, 40, 1118-1140, 2001.
643 Tokay, A., and Short, D. A.: Evidence from tropical raindrop spectra of the origin of rain from
644 stratiform versus convective clouds, Journal of applied meteorology, 35, 355-371, 1996.
645 Ulbrich, C. W.: Natural variations in the analytical form of the raindrop size distribution,
646 Journal of Climate and Applied Meteorology, 22, 1764-1775, 1983.
647 Ulbrich, C. W., and Atlas, D.: Rainfall microphysics and radar properties: Analysis methods
648 for drop size spectra, Journal of Applied Meteorology, 37, 912-923, 1998.
649 Waterman, P.C.: Matrix formulation of electromagnetic scattering. Proc. IEEE, 53, 805-812,
650 1965.
651 Waterman, P.C.: Symmetry, unitarity, and geometry in electromagnetic scattering, Physical
652 review D, 3, 825, 1971.
653 Willis, P. T.: Functional fits to some observed drop size distributions and parameterization of
654 rain, Journal of the Atmospheric Sciences, 41, 1648-1661, 1984.
655 You, C.-H., Lee, D.-I., and Kang, M.-Y.: Rainfall estimation using specific differential phase
656 for the first operational polarimetric radar in Korea, Advances in Meteorology, 2014, 2014.
657

Tables

Tables 1. Specification of POSS disdrometer.

Specifications	Detail
Manufacturer	ANDREW CANADA INC
Module	PROCESSOR
Model number	POSS-F01
Nominal power	100 mW
Bandwidth	Single frequency
Emission	43 mW
Pointing direction	20 ° (to the vertical side)
Antenna	Rectangular pyramidal horns
Range of sample area	< 2 m
Wavelength	10.525 GHz ± 15 GHz
Physical dimension	277×200×200 cm^3
Net weights	Approximately 110 kg

Table 2. Designated date with respect to the source of rainfall.

Rainfall Category	Period			
	2001	**2002**	**2003**	**2004**
Typhoon	-	7.5-7.6, 8.31	5.29, 6.19, 8.7, 9.11-12	6.20, 8.19, 9.6
Changma	6.18-6.19, 6.23-6.26, 6.29-6.30, 7.1, 7.5-7.6 7.11-7.14	6.23-6.25, 6.30, 7.1-7.2	6.12-6.14, 6.23, 6.27 6.30, 7.1, 7.3-7.15	7.11-7.13, 7.14
Heavy rainfall	02.04.15. 20:13 to 02.04.16 06:29			
Seasonal	**Spring**	**Summer**	**Autumn**	**Winter**
	Mar. to May	Jun. to Aug.	Sep. to Nov.	Dec. to Feb.
Diurnal	**DT (KST)**		**NT (KST)**	
	0733 - 1712		1942 - 0509	

680 **Table 3.** Rainfall rate for each rainfall category and the number of sample size for 1-min data.

Rainfall Category	Total precipitation	Stratiform precipitation (%)	Convective precipitation (%)
Typhoon	5095	3118 (61.19)	652 (12.79)
Changma	18526	11099 (59.91)	1611 (8.69)
Heavy rainfall	359	153 (42.61)	150 (41.78)
Spring	30703	20370 (66.34)	1478 (4.81)
Summer	37187	22566 (60.68)	3409 (9.16)
Autumn	19809	12033 (60.74)	850 (4.29)
Winter	11689	7582 (64.86)	339 (2.90)
Daytime	41328	26373 (63.81)	2539 (6.14)
Nighttime	37455	23063 (84.00)	2242 (5.89)
Entire	99388	62551 (62.93)	6076 (6.11)

681

682

683

684

685 **Table 4.** DT and NT (KST) in Summer and Winter season.

Rainfall Category	Period	Beginning time (KST)	Finishing time (KST)
Summer	**DT**	0533	1927
	NT	1942	0509
Winter	**DT**	0733	1712
	NT	1819	0654

686

687

688

689

690

691

692

693

694

695

696

697

698

699

Table 5. Sum of the normalized wind direction frequencies between Summer and Winter.

Sum of the normalized wind direction frequencies				
Season	**Summer**		**Winter**	
Type	**Sea wind**	**Land wind**	**Sea wind**	**Land wind**
Frequency	0.4139	0.5861	0.3137	0.6863
Difference of the normalized wind direction frequency between DT and NT (DT-NT)				
Season	**Summer**		**Winter**	
Type	**Sea wind**	**Land wind**	**Sea wind**	**Land wind**
Frequency	0.0731	-0.0731	-0.0697	0.0697

Figures

Figure 1.

Photograph of the POSS instrument used in this research.

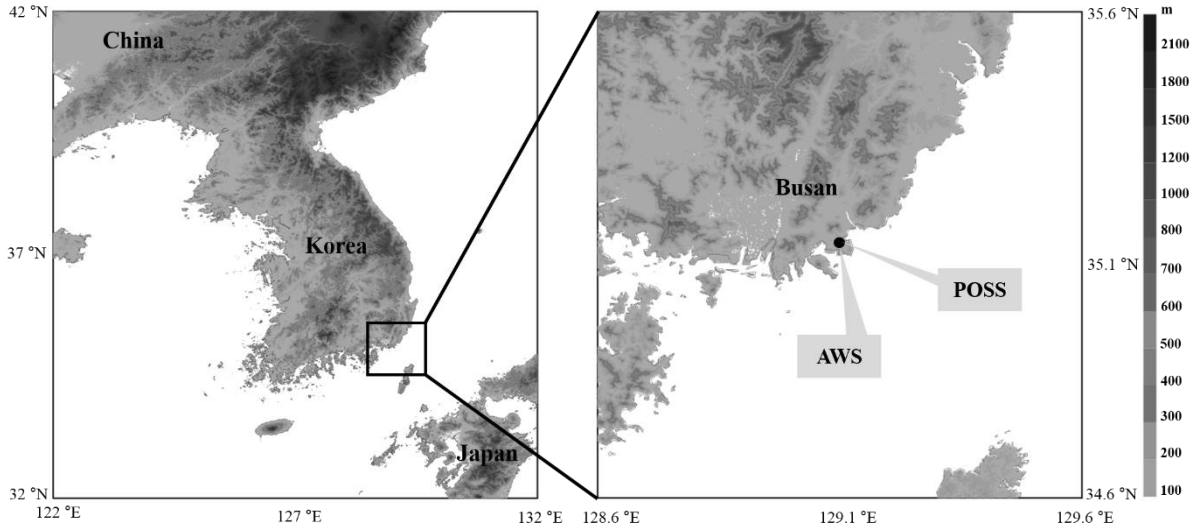

721

722 **Figure 2.**

723 Locations of the POSS and the AWS rain gauge installed in Busan, Korea.

724

725

726

727

728

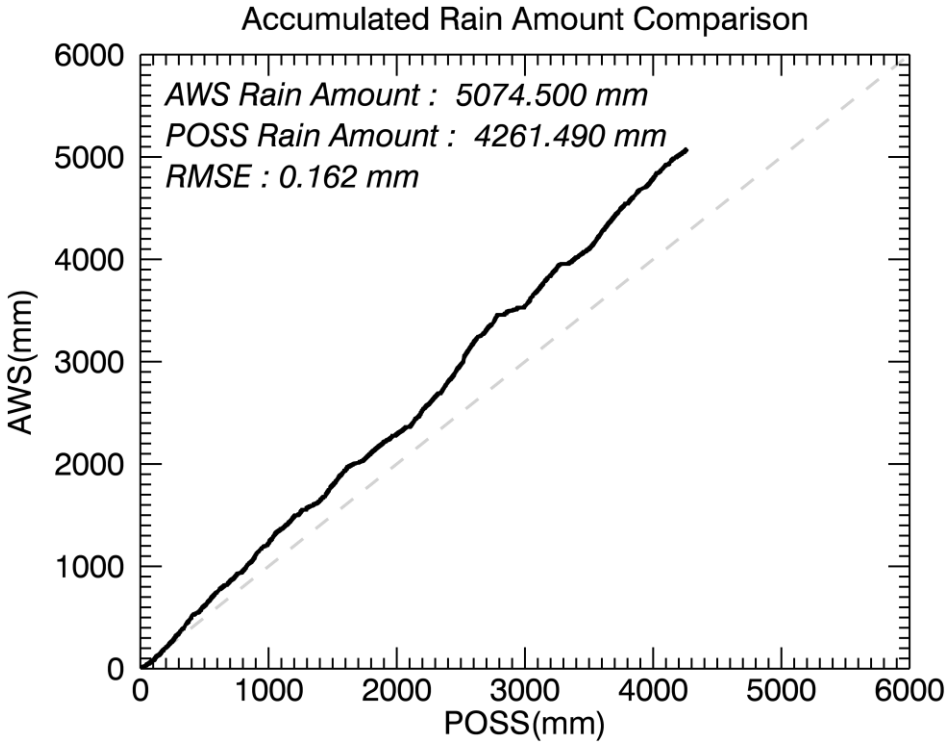

729

730 **Figure 3.**

731 Comparison of the recorded rainfall amounts between the POSS and AWS instrument.

732

733

734

735

736

737

738

739

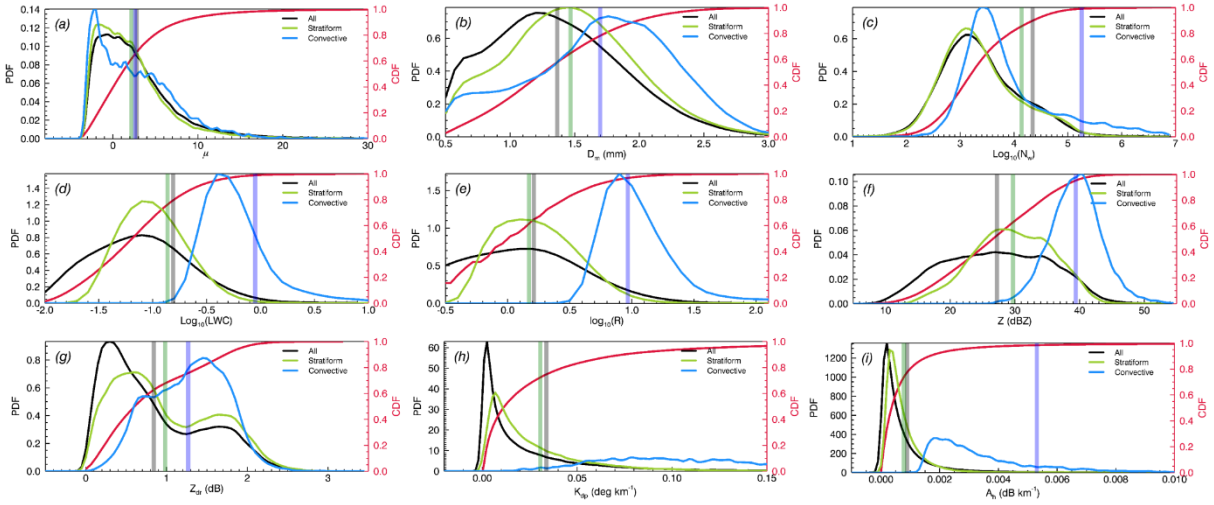

740

741 **Figure 4.**

742 PDF and CDF for (a) μ, (b) D_m, (c) $\log_{10}(N_w)$, (d) $\log_{10}(R)$, (e) $\log_{10}(LWC)$, (f) Z, (g)

743 Z_{dr}, (h) K_{dp}, and (i) A_h for the entire rainfall dataset (solid black line), stratiform rainfall

744 (solid green line), and convective rainfall (solid blue line). The solid red line represents the

745 CDF for entire rainfall dataset. The solid vertical line represents the mean value of each type.

746

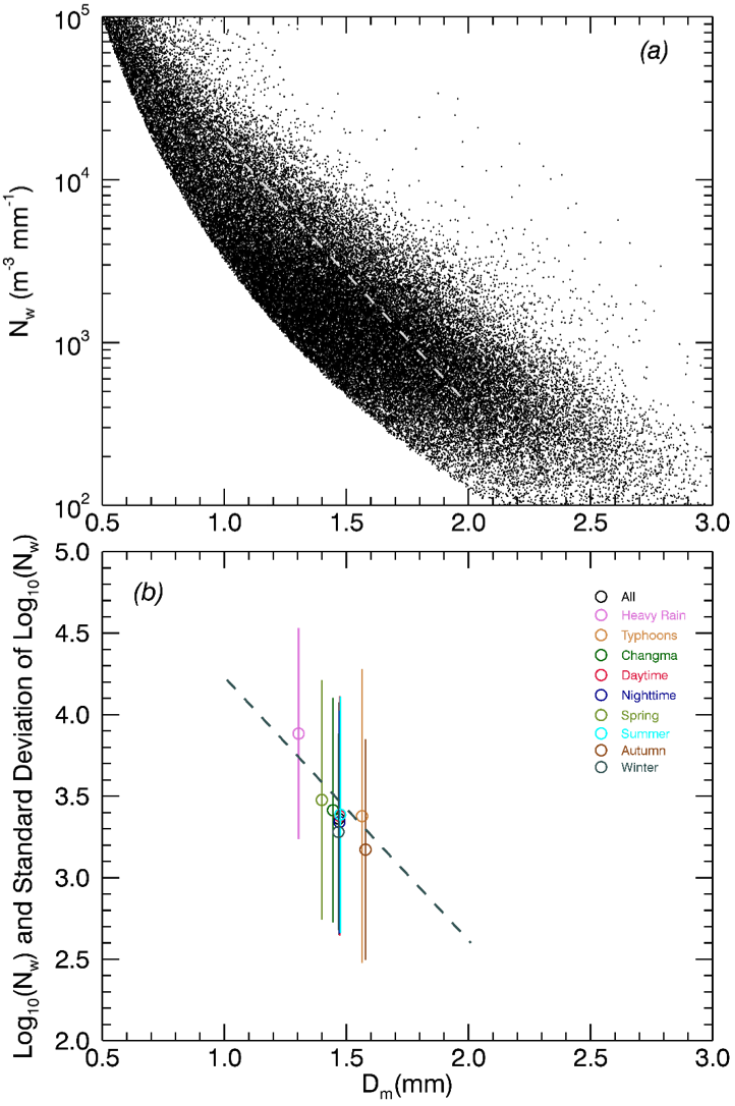

747

748 **Figure 5.**

749 (a) Scatter plot of 1-min D_m and N_w for the 10 rainfall categories with respect to stratiform
750 rainfall data. The broken grey line represents the average line as defined by Bringi et al. (2003).
751 (b) Scatter plot of mean D_m and $\log_{10}(N_w)$ values of the 10 rainfall categories with respect
752 to stratiform rainfall and these mean values for each rainfall type are shown as circle symbols.
753 The vertical line represents $\pm 1\sigma$ of $\log_{10}(N_w)$ for each category.

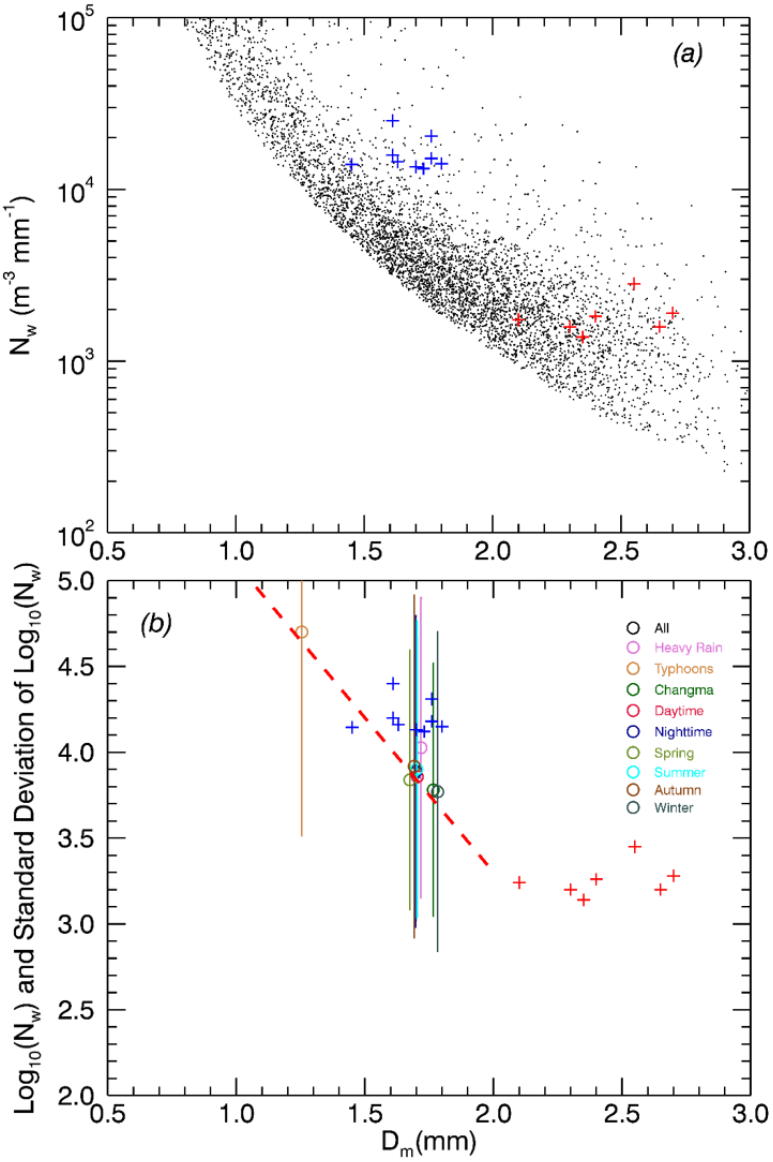

754

755 **Figure 6.**

756 (a) As in Figure 5(a), but for convective rainfall. The blue and red plus symbols represent
757 maritime and continental rainfall, respectively, as defined by Bringi et al. (2003). (b) As in
758 Figure 5(b), but for convective rainfall. The broken red line represents the mathematical
759 expression described in Eq. (16).

760

761

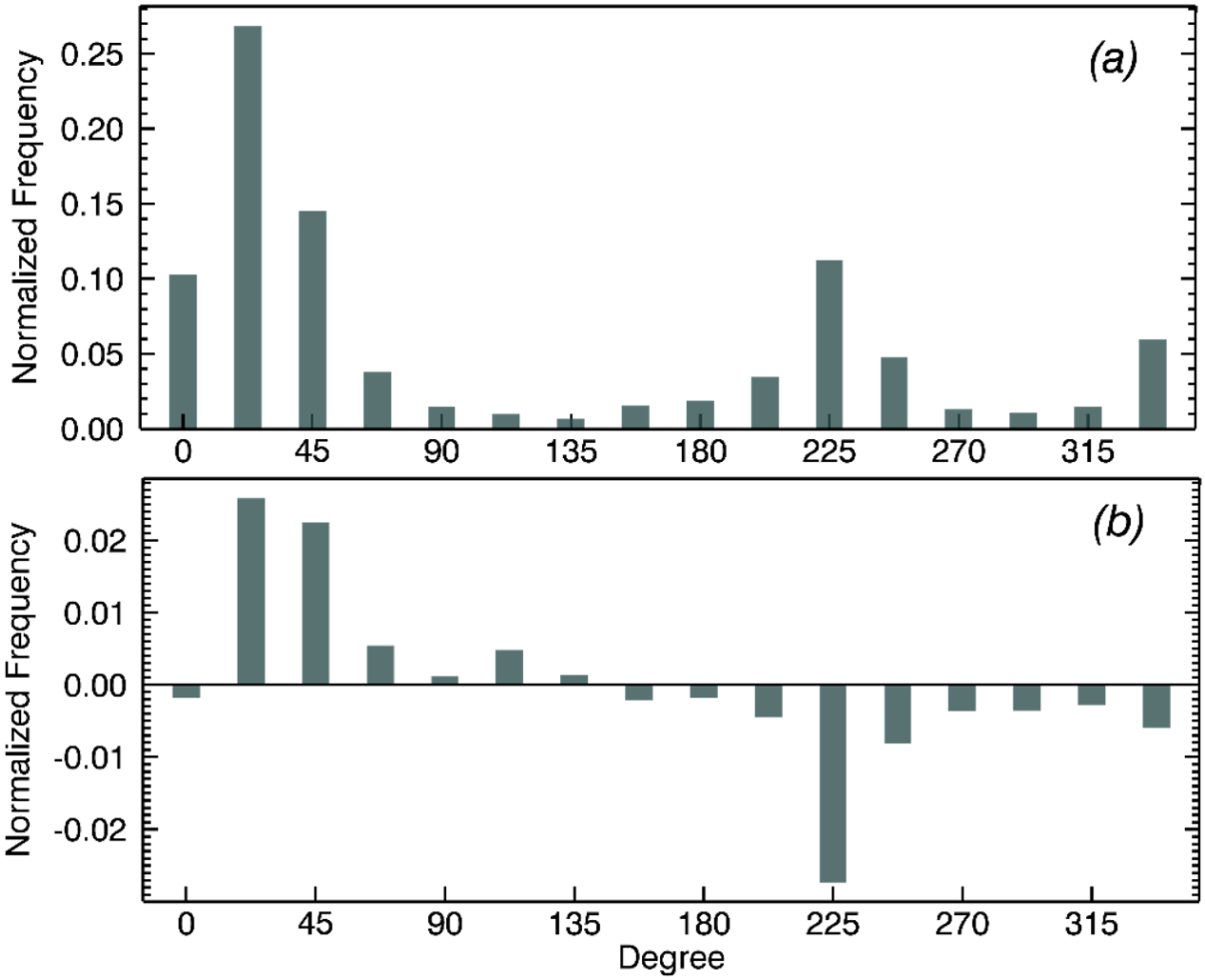

Figure 7.

(a) Histogram of normalized frequency of 16 wind directions for the entire study period. (b) Difference values of wind direction frequencies between DT and NT (DT - NT).

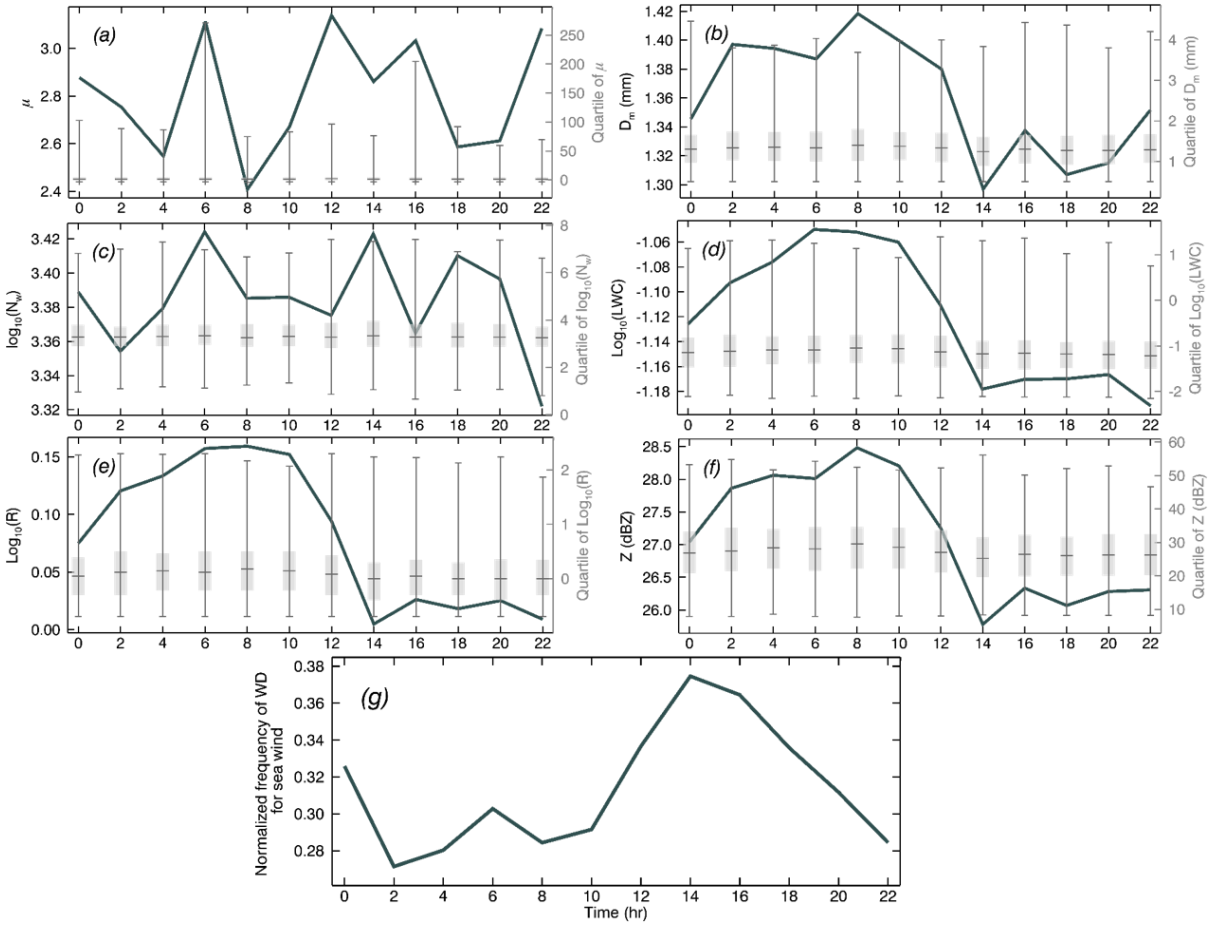

771

772 **Figure 8.**

773 Two hour interval time series of (a) μ, (b) D_m, (c) $\log_{10}(N_w)$, (d) $\log_{10}(R)$, (e)
774 $\log_{10}(LWC)$, (f) Z_h and (g) normalized frequency of wind direction for sea wind (45° to 225°)
775 with quartiles for the total period. Solid lines are quartiles for each time.

776

777

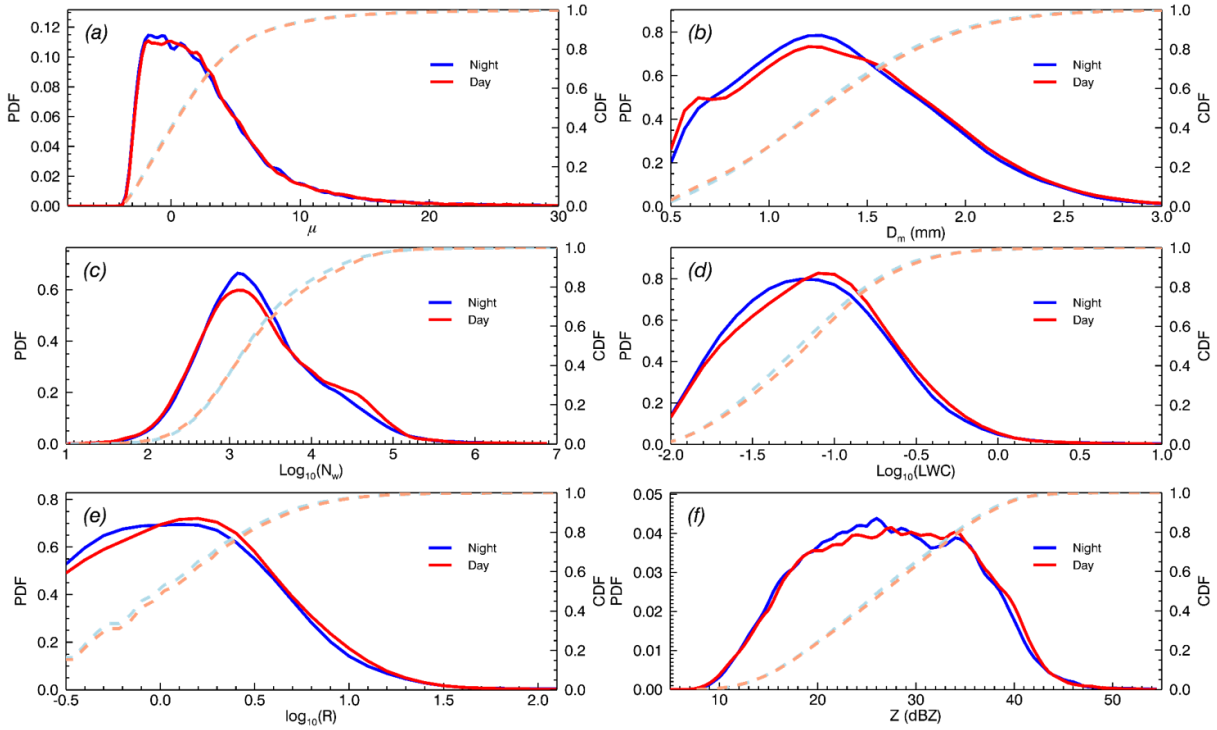

778

779 **Figure 9.**

780 PDF and CDF curves for (a) μ, (b) D_m, (c) $\log_{10}(N_w)$, (d) $\log_{10}(R)$, (e) $\log_{10}(LWC)$, and

781 (f) Z for DT and NT according to the entire period. The solid red and blue lines represent the

782 PDF for DT and NT, respectively. The broken light red and blue lines represent the CDF for

783 DT and NT, respectively.

784

785

786

787

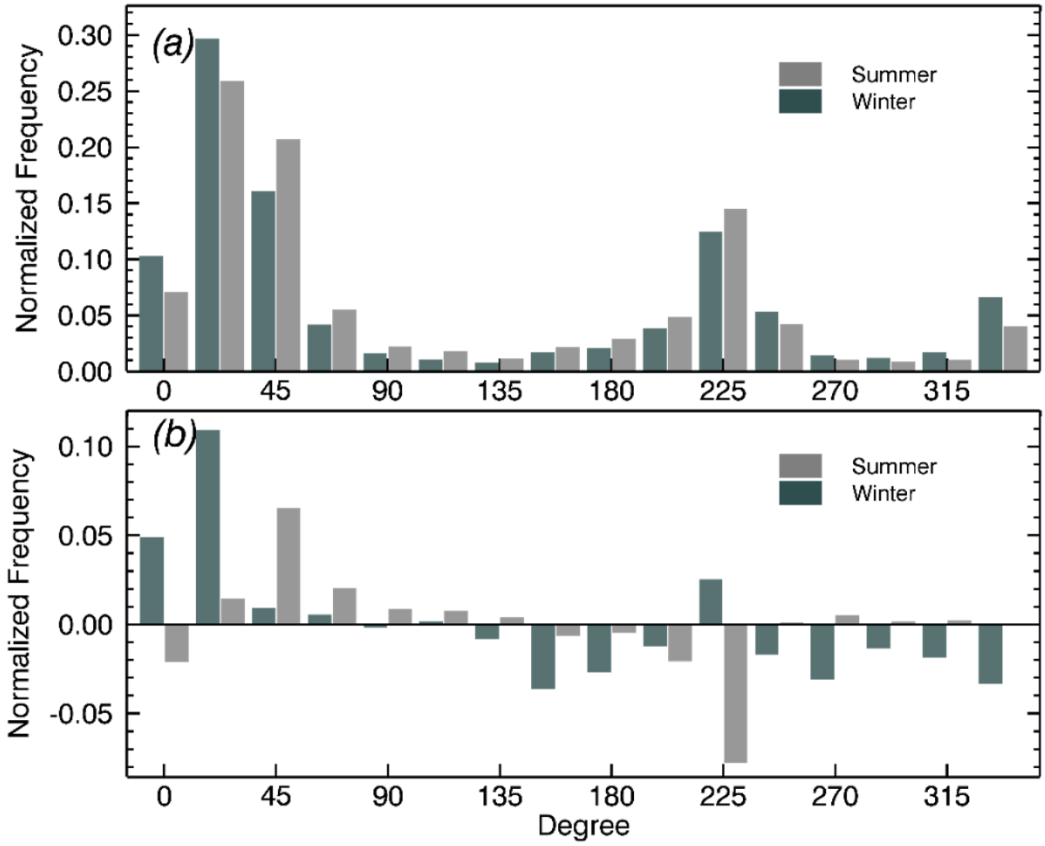

Figure 10.

Histogram of normalized frequency for 16 wind directions in (a) the entire period and (b) differences of normalized frequency with respect to wind directions between DT and NT (DT – NT) for Summer (light grey) and Winter (dark grey) season.

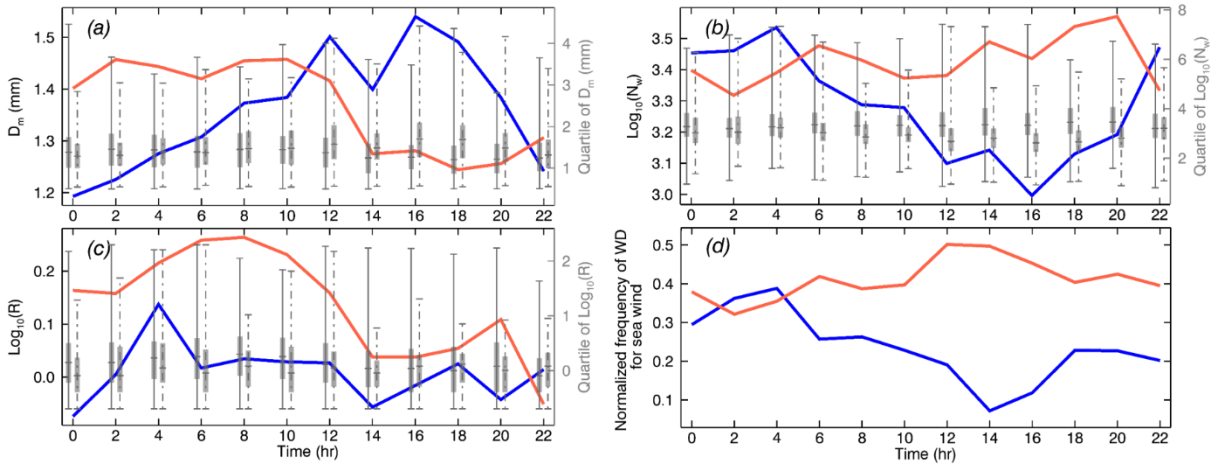

798

799 **Figure 11.**

800 Two hour interval time series and quartiles of (a) D_m, (b) $\log_{10}(N_w)$ (c) $\log_{10}(R)$ and (d)
801 normalized frequency of wind direction for sea wind (45° to 225°) for the Summer (red) and
802 Winter (blue) season. Solid (broken) lines are quartiles of Summer (Winter) for each time,
803 respectively.

804

805

806

807

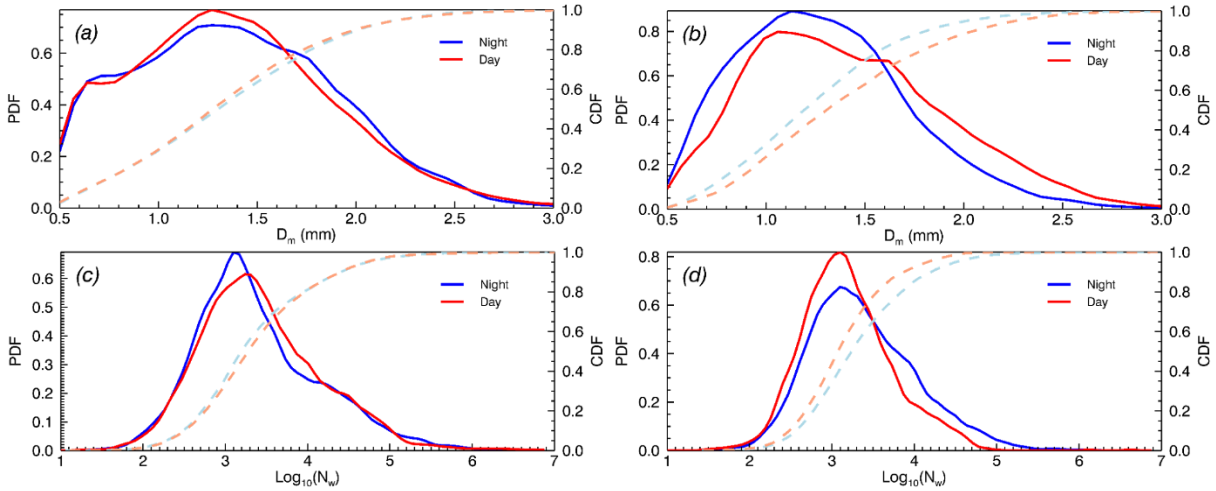

Figure 12.

PDF and CDF of (a) D_m ((b) D_m) and (c) N_w ((d) N_w) for the entire rainfall type in the Summer (Winter) season. Red and blue solid lines represent the PDF of DT and NT, respectively. The light red and blue broken lines represent the CDF for each season

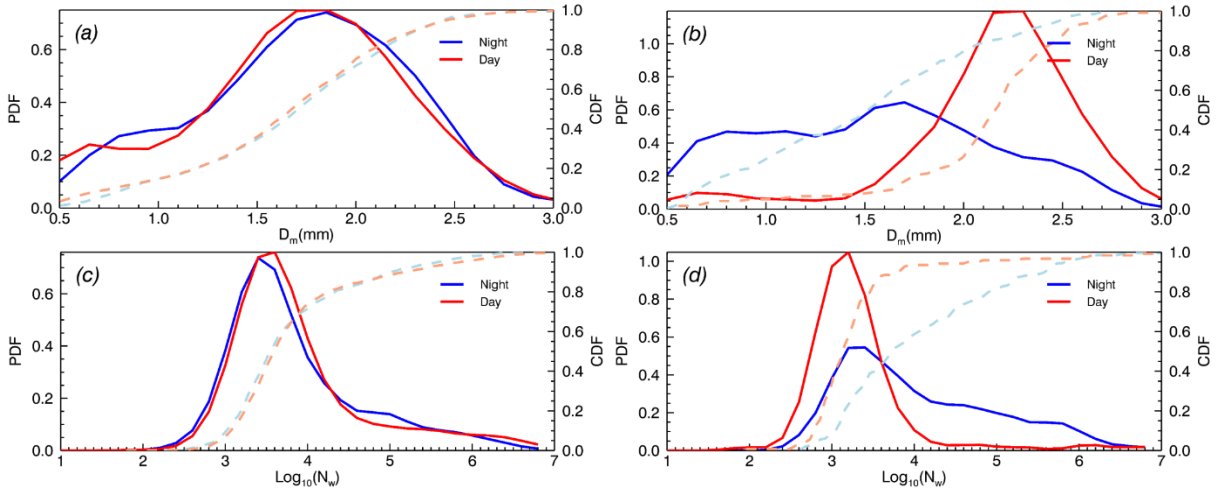

Figure 13.

As in Figure 12, but for convective rainfall type.